Journal of Biomedical Optics

SPIEDigitalLibrary.org/jbo

Using ultrahigh sensitive optical microangiography to achieve comprehensive depth resolved microvasculature mapping for human retina

Lin An
Tueng T. Shen
Ruikang K. Wang

SPIE

Using ultrahigh sensitive optical microangiography to achieve comprehensive depth resolved microvasculature mapping for human retina

Lin An,[a] Tueng T. Shen,[a,b] and Ruikang K. Wang[a,b]
[a]University of Washington, Department of Bioengineering, Seattle, Washington 98195
[b]University of Washington, Department of Ophthalmology, Seattle, Washington 98104

Abstract. This paper presents comprehensive and depth-resolved retinal microvasculature images within human retina achieved by a newly developed ultrahigh sensitive optical microangiography (UHS-OMAG) system. Due to its high flow sensitivity, UHS-OMAG is much more sensitive to tissue motion due to the involuntary movement of the human eye and head compared to the traditional OMAG system. To mitigate these motion artifacts on final imaging results, we propose a new phase compensation algorithm in which the traditional phase-compensation algorithm is repeatedly used to efficiently minimize the motion artifacts. Comparatively, this new algorithm demonstrates at least 8 to 25 times higher motion tolerability, critical for the UHS-OMAG system to achieve retinal microvasculature images with high quality. Furthermore, the new UHS-OMAG system employs a high speed line scan CMOS camera (240 kHz A-line scan rate) to capture 500 A-lines for one B-frame at a 400 Hz frame rate. With this system, we performed a series of *in vivo* experiments to visualize the retinal microvasculature in humans. Two featured imaging protocols are utilized. The first is of the low lateral resolution (16 μm) and a wide field of view (4×3 mm^2 with single scan and 7×8 mm^2 for multiple scans), while the second is of the high lateral resolution (5 μm) and a narrow field of view (1.5×1.2 mm^2 with single scan). The great imaging performance delivered by our system suggests that UHS-OMAG can be a promising noninvasive alternative to the current clinical retinal microvasculature imaging techniques for the diagnosis of eye diseases with significant vascular involvement, such as diabetic retinopathy and age-related macular degeneration. © *2011 Society of Photo-Optical Instrumentation Engineers (SPIE).*
[DOI: 10.1117/1.3642638]

Keywords: microvasculature imaging; retinal imaging; optical microangiography; spectral domain optical coherence tomography.

Paper 11422R received Aug. 3, 2011; revised manuscript received Aug. 28, 2011; accepted for publication Sep. 2, 2011; published online Oct. 24, 2011.

1 Introduction

Being one of the most energy demanding (per gram basis) organs in the human body, the retina depends on a finely organized complex microvasculature system for the supply of necessary nutrients and the clearance of metabolic by-products to maintain healthy functional vision activities.[1] Even a small change of the retinal microvasculature may cause a deleterious effect on visual functions. Increasingly more evidence has suggested that the abnormal states of the retinal vasculature may lead to irreversible vision loss, such as diabetic retinopathy, vascular occlusion, and age-related macular degeneration.[2–4] Better assessment of the retinal microvascular dynamics is important to provide critical diagnostic information for physicians. Currently, the standard diagnostic tool for visualizing the retinal blood vessel network is fluorescein angiography (FA). Through collecting the fluorescence light emitted from the contrast agent (sodium fluorescein dye), FA is capable of providing detailed retinal vasculature images. However, it requires the injection of a contrast agent into the blood stream, which is uncomfortable and sometimes may cause adverse allergic reactions, such as nausea and itching. Additionally, FA cannot provide valuable depth information for vessel localizations.

Because of its attractive features, e.g., noninvasiveness, contactless, depth-resolved localization, and high resolution, optical coherence tomography (OCT)[5] has become widely used in ophthalmic clinic as an important diagnostic tool.[6,7] Based on OCT technology, a number of useful imaging modalities have been proposed in order to isolate the blood flow signals from biological tissue, e.g., Refs. 8–21, and 22. Among these methods, phase-resolved optical Doppler tomography (PRODT)[8] is the most notable, in which the phase difference between adjacent A-lines is used to evaluate the flow information. However, this method is only sensitive to the axial velocity of the flow due to the limitation of Doppler effect. It is currently still a formidable task for PRODT to provide retinal microvasculature mapping because the probe beam is almost perpendicular to the vasculature network orientation, in addition to the tissue noise background[23] that reduces the system sensitivity to the blood flow. To improve the sensitivity of the PRODT method, there are a number of useful strategies that have been proposed by several research groups. For example, Makita et al. proposed a dual-beam-scan Doppler OCT imaging technique, which is able to significantly increase the system sensitivity while maintaining the nature of high imaging speed for the system.[24,25] Another approach is to use the phase variance method, which was originally proposed by Zhao et al. to calculate the lateral velocity information.[8]

Address all correspondence to: Ruikang K. Wang, University of Washington, Dept of Bioengineering, 3720 15th Ave. NE, Seattle, Washington 98195; Tel: 206 616 5025; FAX: 206 685 3300; E-mail: wangrk@uw.edu.

1083-3668/2011/16(10)/106013/9/$25.00 © 2011 SPIE

When applied between adjacent B-frames, this method has been reported to achieve microcirculation mapping within retina.[19] However, both of these methods are phase-based techniques. It is known that the phase stability of the optical system is directly determined by the signal-to-noise ratio (SNR) of the OCT signal,[15] thus, a relatively lower SNR would have a significant impact on the noise level of the final flow images.

Recently, another novel OCT-based blood flow imaging modality, optical microangiography (OMAG) was proposed,[26] which has been demonstrated to deliver a markedly better imaging performance compared to the currently available methods. As a variation of OCT technology, OMAG is capable of producing noninvasive three-dimensional (3D) blood vessel distribution maps with high resolution for the living biological tissue. Its physical principle is based on the well-known Doppler effect, and to a lesser extent on the dynamic speckle caused by the moving particles. Through analyzing the Doppler beating frequency carried by the light backscattered from the moving particles, OMAG is able to isolate the blood flow signals from the static background tissue. Unlike the phase-based approaches, OMAG directly analyzes the complex interferogram to produce the imaging contrast, which essentially minimizes the instability coming from the phase noise.[15] Since reported, OMAG has been successfully applied to visualize the human ocular vasculature map.[27–29] However, as to *in vivo* human applications, it is difficult, if not impossible, for the traditional OMAG to achieve high enough sensitivity for visualizing the retinal capillary blood vessels because the algorithm was applied to the fast scan direction, leading to a relatively short time interval between adjacent A-lines.[30] To increase the system sensitivity, a novel extension, ultrahigh sensitivity OMAG (UHS-OMAG) was proposed to achieve ~4 μm/s flow sensitivity through applying the OMAG algorithm onto the slow scanning axis.[30] The reason behind this dramatic improvement of the system sensitivity to the blood flow is simple because the OMAG algorithm is now applied to the adjacent B-scans, leading to an order of magnitude increase of the time-interval for sampling the slow motion. Applying this novel approach, a detailed microvasculature network of human retina was achieved.[31] However, there are still at least two shortcomings that can degrade significantly the final imaging performance for our preliminary system reported in Ref. 31. The first one is the motion artifacts coming from the movements of a human eye and head, which is inevitable during imaging. Previously in Ref. 32, a phase compensation method used in Ref. 27 was applied to mitigate the motion artifacts. However, the successful implementation of this phase compensation method requires that the axial components of bulk tissue movement may not exceed the maximum detectable velocity determined by the time interval between B-scans. Otherwise, the calculated phase value for compensation does not accurately represent the velocity caused by the tissue bulk motion. Because of the relatively longer time interval (2.5 ms in our previous UHS-OMAG system), the maximum compensable movement is only ~0.17 mm/s, which is small compared to human eye or head movements. This practical problem makes it difficult for the system to obtain a high quality flow image from an untrained patient. Another shortcoming is the relatively slow imaging speed of the system, which was reported at ~140 kHz. When the fast-scanning speed was set at 400 Hz, the previous system could only capture 256 A-lines to form one B-scan. As a consequence, in order to obtain microvasculature images with acceptable quality, we had to reduce the imaging window size (i.e., the field of view) to achieve a high enough A-line density in one B-frame image.

In this paper, we report a newly developed high-speed UHS-OMAG system that is capable of achieving a detailed microvasculature network of human retina *in vivo* with tolerable motion artifacts. A novel phase compensation method, i.e., a high order phase compensation method, is proposed to significantly extend the capability of the previous approach to compensate the motion artifacts. A faster line scan CMOS is employed to provide the system with a 240 kHz A-line rate that reduced the total imaging time period. Based on the current system, we designed two types of imaging modes for visualizing the retinal microvasculature network. The first imaging mode has a large field of view but with a relatively lower lateral resolution to visualize the retinal microvasculature within a large area on the posterior segment of the human eye. The second one is an imaging mode that has higher lateral resolution that is used to achieve very detailed visualization of retinal blood vessels, including capillaries, albeit within a smaller examining window. The images obtained from both imaging modes were segmented into three different layers for visualizing the retinal microvasculature located at different depth positions.

2 System Configuration

The schematic of our system is illustrated in Fig. 1. The light source was a superluminescent diode, emitting a broadband light with 842 nm central wavelength and 46 nm bandwidth, which gave a ~8 μm axial resolution in the air. The output light was delivered to a 20/80 fiber coupler and split into the sample arm (20% light) and the reference arm (80% light). In the reference arm, a 20 mm water cell was used to compensate the dispersion caused by the human eye. The lights backscattered from the eye and reflected from the reference mirror were recombined at the fiber coupler and delivered into a home-built high speed spectrometer which consisted of a transmission grating (1200 lines/mm), an achromatic focusing lens (100 mm focal length), and a high speed line scan CMOS camera (Basler, Sprint spL4096-140 k). The designed spectral resolution of the spectrometer was ~0.65 nm, providing ~2.5 mm imaging depth on both sides of a zero delay line. For the imaging studies reported in this paper, the exposure time of the camera was set at 2.9 μs and the active pixel numbers in the camera was set at 896, enabling a ~240 kHz line scan rate for imaging.

Depending on the requirements of the imaging goals, such as the field of view and lateral resolution, we used different sample arm configurations and scanning protocols. The first goal of our study aimed at providing a larger field of view of the retinal vasculature map. To achieve this goal, the beam diameter after the ocular lens in the sample arm was configured at ~1.5 mm that provided ~16 μm lateral resolution on the retina. In the fast-scan (X) direction, 500 A-lines with ~8 μm spatial interval between adjacent A-scans was used to form one B-scan image, which covered ~4 mm on the retina. In the slow-scan (Y) direction, 250 locations were scanned to cover ~3 mm on the retina. In each location, 5 B-frames were acquired. The imaging rate was 400 frames per second. Thus, it took ~3 s to complete

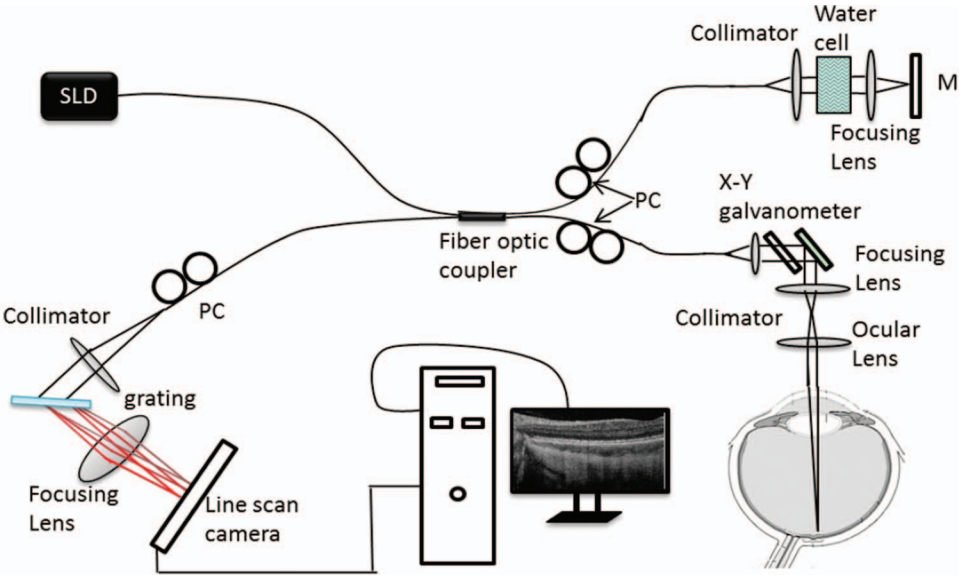

Fig. 1 Schematic of UHS-OMAG system. SLD: superluminescent diode; PC: polarization controller.

one C-scan (3D) image, which time period is suitable for *in vivo* imaging applications. For further increasing the field of view, we sequentially scanned six different areas (two in the *X*-direction and three in the *Y*-direction). And then these six scans were stitched together to form a wide field of microvasculature map covering $\sim 7 \times 8$ mm^2 on the human retina.

The second goal of our study was to achieve localized high resolution vasculature images for detailed visualization of retinal vessel morphologies, including capillaries. To realize this, the sample beam diameter on the cornea was configured to be $\sim$5 mm, which provided $\sim$5 μm lateral resolution on the retina. With this imaging resolution, the scanning ranges of the above scanning protocol were adjusted to be 1.5 mm in the *X*-direction and 1.2 mm in the *Y*-direction.

Based on the depth-resolved capability provided by the FDOCT technology, the final OMAG flow images can be segmented into land-marked depth layers, e.g., the ganglion cell layer (GCL), the inner plexiform layer (IPL), and the outer plexiform layer (OPL), according to their depth positions. To segment these layers, we used the same method presented in our previous work.[31,32] Briefly speaking, the retinal pigment epithelium (RPE) layer was first identified as the reference of the segmentation. The layer that is $\sim$425 μm above the RPE was labeled as the GCL. The layer located between 300 and 425 μm above the RPE was labeled as the IPL. The layer lying between 50 and 300 μm above the RPE was labeled as the OPL. After segmentation, the maximum amplitude projection was performed along the depth direction to the obtained depth-encoded microvasculature maps within the retina.

3 High Order Phase Compensation to Reduce Bulk Motion Artifacts

The detailed description of UHS-OMAG has already been given in Refs. 30 and 31. Theoretically, as discussed in Refs. 30 and 32, a simplified version of the interferogram captured by the UHS-OMAG system that ignores all the components that do not contribute to the useful information about microstructure and flow can be presented as:

$$I(t,k) = 2S(t,k)E_R \int_{-\infty}^{\infty} a(z,t)\cos[2kn(t)(z-vt)]dz, \qquad (1)$$

where k is the wavenumber of the light; t is the time when the interferogram was captured; $I(t, k)$ is the light intensity; E_R is the light reflected from the reference mirror; $S(t, k)$ is the spectral density of the light source used; n is the refractive index; z is the depth; $a(z, t)$ is the amplitude of the backscattered light; and v is the velocity of the moving blood cells, which generates the Doppler beating frequency in the interferogram. To isolate the slow flow signals, the OMAG algorithm is applied onto the slow scanning axis (Y direction), which takes advantage of the relatively long time-interval between two B-frames to achieve ultrahigh velocity sensitivity to the blood flow.

During the *in vivo* imaging of the microvasculature network within the human retina, the motion artifacts caused by the movements of a human eye or head pose a significant challenge for obtaining a high quality image of blood vessels. To reduce the motion artifacts on the final imaging results, in our previous work,[31,32] a phase compensation method proposed in Ref. 27 was directly inherited to improve the imaging performance of the UHS-OMAG system. This prior method was based on the accurate estimation of the velocity due to the bulk tissue motion through the use of the algorithm usefully applied in Doppler OCT. However, because of the relatively longer time interval ($\sim$2.5 ms), the unambiguous velocity that can be determined is only $\sim$0.17 mm/s in both directions, which is small under the circumstances of *in vivo* human imaging applications. Though the images with high quality can be achieved on healthy and well trained volunteers, the strict experimental requirement as mentioned above makes it difficult to be fulfilled when imaging is performed on untrained patients. A better solution to mitigate the problem imposed by the relatively large tissue motion is thus needed for imaging the patients.

Considering the raw interferogram captured by the UHS-OMAG system [i.e., Eq. (1)], the simplified version of the

analytical signals at each B-frame could be expressed by the following equation after applying the Fourier transformation onto Eq. (1) along the z direction:

$$\tilde{B}(n,z) = A(n,z)\exp[i\phi(n,z)], \tag{2}$$

where n is the index of B-scans; z is the depth position; and A and Φ are the magnitude and phase of the analytical function. If the bulk motion happens, through comparing adjacent two B-frames, the phase difference can be presented as:

$$\Delta\phi_B(n) = \phi(n,z) - \phi(n-1,z), \tag{3}$$

where $\Delta\Phi_B$ is the phase difference generated by the bulk tissue motion that is required for compensating the motion artifacts. Here, we ignore the phase difference term generated by the moving particles, which could be easily eliminated through an averaging process[27] or a histogram-based phase selecting process.[12] Note that the description that follows can be easily appreciated by considering that the evaluated phase from a complex function is always nested within $[-\pi, \pi]$, i.e., we have access only to the phase modulo 2π.

The evaluated phase difference $\Delta\Phi_B(n)$ is directly related to the real axial velocity of the eye or head movements through the following equation:

$$v = \frac{\lambda_0\Delta\phi_B}{4\pi n\Delta t} \pm m\frac{\lambda_0}{4n\Delta t}, m = 0, 1, 2\ldots, \tag{4}$$

where λ_0 is the central wavelength and Δt is the time interval between adjacent B-frames acquired by the UHS-OMAG system. When the axial velocity imposed by the bulk tissue motion satisfies the condition $-\lambda_0/4n\Delta t < v < \lambda_0/4n\Delta t$, it can be determined from phase $\Delta\Phi_B$ without any ambiguity because there is no phase wrapping occurring (i.e., $m = 0$). In this case, Eq. (2) can be rewritten as:

$$\tilde{B}(n,z) = A(n,z)\exp\{i[\phi(n-1,z) + \Delta\phi_B(n)]\}. \tag{5}$$

Thus, the evaluated phase $\Delta\Phi_B$ between adjacent B-frames can be directly plugged into Eq. (5) to eliminate the phase caused by the tissue motion. In fact, this is the process that the prior phase-compensation method was employed.

However, for a velocity that is large enough to cause phase wrapping (i.e., $m > 0$) between adjacent B-frames, the evaluated phase $\Delta\Phi_B$ is no longer able to provide a good estimation for the real velocity caused by bulk tissue motion because of the existence of the phase ambiguity. Depending on the value of bulk tissue motion velocity, there are two different scenarios for this phase ambiguity. First, if its value satisfies $v = \lambda_0\Delta\phi_B/4\pi n\Delta t \pm 2m(\lambda_0/4n\Delta t)(m = 1, 2, 3\ldots)$, the real phase generated by the bulk tissue motion should be $\Delta\Phi_{rB}(n) = \Delta\Phi_B(n) \pm 2m\pi$. In this case, the analytical interferogram in Eq. (5) should be rewritten as:

$$\tilde{B}(n,z) = A(n,z)\exp\{i[\phi(n-1,z) + \Delta\phi_B(n) \pm 2m\pi]\}. \tag{6}$$

It is clear that Eq. (6) can be theoretically represented by Eq. (5), even though the ambiguity $2\,m\pi$ exists. Thus, the calculated phase $\Delta\Phi_B$ is still good for phase compensation to achieve satisfactory results.

On the other hand however, if $v = \lambda_0\Delta\phi_B/4\pi n\Delta t \pm (2m-1)(\lambda_0/4n\Delta t)(m = 1, 2, 3\ldots)$, the real phase generated by the bulk motion now becomes $\Delta\Phi_{rB}(n) = \Delta\Phi_B(n) \pm (2m\text{-}1)\pi$. Under this circumstance, the analytical interferogram in Eq. (5) should be rewritten as:

$$\tilde{B}(n,z) = A(n,z)\exp\{i[\phi(n-1,z) + \pi - \Delta\phi_B(n) \pm 2m\pi]\}. \tag{7}$$

If we still use the calculated phase $\Delta\Phi_B(n)$ to compensate Eq. (5), then it would become:

$$\tilde{B}(n,z) = A(n,z)\exp\{i[\phi(n-1,z) + \pi - 2\Delta\phi_B(n) \pm 2m\pi]\}. \tag{8}$$

It is now clear that such treatment of phase compensation fails to achieve good performance because the compensated interferogram still possesses the phase residual that comes from the tissue motion.

To solve this issue, let us look at Eq. (8) carefully. If $|2\Delta\Phi_B(n)| > \pi$, then Eq. (8) can be written as:

$$\tilde{B}(n,z) = A(n,z)\exp\{i[\phi(n-1,z) + R_1\phi_B(n) \pm 2m\pi]\}, \tag{9}$$

where $R_1\Delta\Phi_B(n) = \pi\text{-}\,|2\Delta\Phi_B(n)|$. As we noticed, Eq. (9) is identical to Eq. (6). Thus, this residual phase $R_1\Delta\Phi_B(n)$ can be compensated if we perform the phase-compensation method one more time.

However, if $|2\Delta\Phi_B(n)| < \pi$, the calculated phase difference value from Eq. (8) will become $2\Delta\Phi_B$. Another iteration of compensation to Eq. (8) will make the interferogram become:

$$\tilde{B}(n,z) = A(n,z)\exp\{i[\phi(n-1,z) + \pi - 4\Delta\phi_B(n) \pm 2m\pi]\}. \tag{10}$$

Thus, after the compensation process is applied n times, the resulting analytical signal becomes:

$$\tilde{B}(n,z) = A(n,z)\exp\{i[\phi(n-1,z) + \pi - 2^{n-1}\Delta\phi_B(n) \pm 2m\pi\}. \tag{11}$$

This process is continued until $|2^{n\text{-}1}\Delta\Phi_B(n)| > \pi$ is satisfied. At this stage, Eq. (11) could also be written as:

$$\tilde{B}(n,z) = A(n,z)\exp\{i[\phi(n-1,z) + R\phi_B(n) \pm 2m\pi\}, \tag{12}$$

where $R\Delta\Phi_B(n) = \pi\text{-}\,|2^{n\text{-}1}\Delta\Phi_B(n)|$. Now, the format of the analytical signal of Eq. (12) becomes identical to Eq. (6). As a consequence, a final iteration of the phase-compensation operation leads to the residual phase $R\Delta\Phi_B(n)$ being compensated.

In essence, the high order phase compensation method actually works to apply the traditional phase compensation method for multiple times. How many iterations are needed to achieve satisfactory performance depends on how severe the bulk motion is. Once the bulk motion was compensated, its calculated phase difference value will always be around zero. Further iteration of phase compensation will no longer have an effect on the final results. Theoretically, the higher order the compensation process is applied, the better is the imaging performance that the system can achieve. However, the high order process will increase the processing time. Empirically, we used an order of four to process the data, which could provide good enough tolerance to the bulk motion with acceptable computational time.

Though the high order phase compensation algorithm is able to break through the phase ambiguity limitation, its performance is still limited by a correlation requirement between the adjacent B-frames. For relatively large bulk tissue motion, once the movements during the time interval between two B-frames exceed the probe beam spot size on the sample, the correlations between two frames will be totally broken, making the calculated phase value unreliable. In this case, the high order phase

compensation method is no longer valid. Empirically, as long as the movement is less than two-thirds of the probe beam spot size, the phase-compensation approach is efficient to improve the imaging quality of the UHS-OMAG system. Considering the setup of the UHS-OMAG system, the probe beam spot size is ~16 μm for the low-resolution imaging protocol, meaning that the limitation of the phase compensation method for a tissue motion velocity is ~4.2 mm/s. This value is more than 25 times higher than the traditional phase-compensation method. For the high-resolution imaging mode with a spatial resolution of ~5 μm, the tolerance for a tissue motion is ~1.3 mm/s, still about ~8 times higher than the traditional approach.

4 *In Vivo* Experiments and Imaging Protocols

To demonstrate the capability of the high speed UHS-OMAG system, we performed experiments by imaging retinal microvasculature of a healthy, but untrained volunteer. During the experiments, the head of the volunteer was positioned on a home-built ophthalmology stage in order to minimize the head movement. An aiming light was introduced in the system to help minimize the movement of the human eye. The whole processes of the experiments were performed in a dark room to help the dilation of the human pupil but without any pupil dilation drug applied.

Before imaging, the traditional FDOCT scanning was first performed to obtain a large field of view (~9×9 mm^2 on the retina), resulting in an OCT fundus image that was used to illustrate the scanning locations for the UHS-OMAG experiments. To obtain the OCT fundus image, 512 A-lines were captured to form one B-scan along the fast-scan direction and 512 B-frames were captured along the slow-scan direction. The OCT signals were then integrated along the depth direction to produce the image contrast.[9] Figure 2 gives such OCT fundus image.

To illustrate the efficiency of the high order phase compensation method, experiments were performed to acquire two-dimensional cross sectional images. In the experiments, 500 A-lines were captured within one B-scan to cover ~4 mm in the *X*-direction (i.e., fast scan). Then B-scans were repeatedly acquired at the same location at the 400 Hz frame rate (the scanning location was marked by the dashed line in Fig. 2).

To demonstrate the microvasculature imaging capability of the UHS-OMAG system, we used two imaging protocols. The first one was a mode that gives a large field of view. A 3D data set was captured around the macular region. This experiment utilized the low resolution probe in the sample arm to scan ~4×3 mm^2 around the fovea region (the location is marked by the larger dashed square in Fig. 2).

To further increase the field of view of the UHS-OMAG system, we scanned six different areas around the macular region (indicated by the solid square in Fig. 2, the numbers represent the scanning order). After imaging, we stitched those six images in order to form a microvasculature imaging that represents an area of ~7×8 mm^2 on the retina. The whole imaging process for this experiment lasted ~1 min, with a resting period of a couple of seconds between adjacent scanning.

Though the above experiments could obtain abundant information about the microvasculature networks within human retina in a large field of view, it is difficult to resolve very fine microvessels, particularly the capillaries, because the spatial resolution was only ~16 μm. The average diameter of capillaries

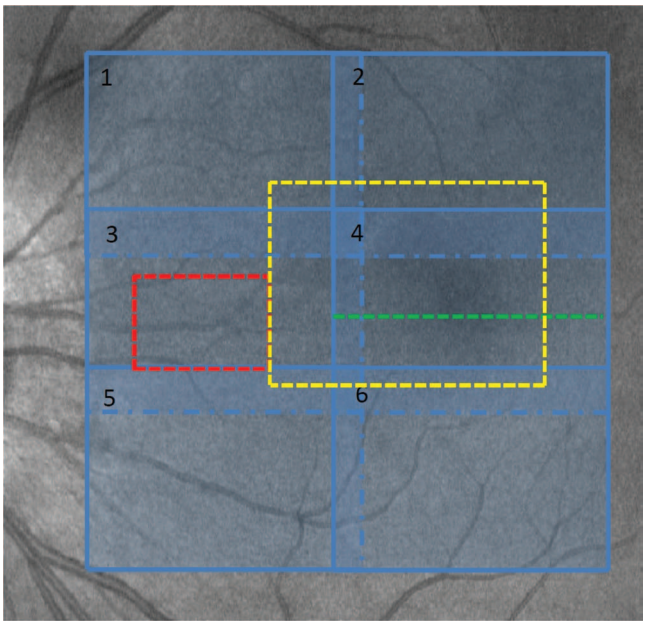

Fig. 2 FDOCT fundus image. Larger dashed square indicates the region where a typical UHS-OMAG 3D data was captured. Solid square indicate the scanning positions for imaging a large field of view (the number represents the scanning order); the region marked with small dashed square corresponds to the imaging location for high resolution imaging protocol; the dashed line marks the position of a typical B-scan cross section image.

is between 6 and 8 μm, thus in order to resolve the capillaries, the spatial resolution of the system must be increased. To meet this requirement, we applied the second imaging protocol, i.e., a high resolution imaging mode. In this mode, the spatial resolution was ~5 μm. Because of the decreased imaging spot size on the retina, the imaging area was also reduced to ~1.5 $\times$ 1.2 mm^2 (indicated by the small dashed square in Fig. 2).

5 Results

5.1 *Effect of the Proposed Phase-Compensation Method*

Figure 3 illustrates typical cross-sectional imaging results obtained by the current UHS-OMAG system, captured from a location marked by the green line in Fig. 2. Figure 3(a) is the cross sectional structure image of the selected location, from which three layers (GCL, IPL, and OPL) at different depth positions can be clearly identified. Applying the UHS-OMAG algorithm along the slow axis, the optical signals backscattered from moving blood cells within microblood vessels buried within the tissue bed can be isolated.

Figure 3(b) is the phase difference map between successive B-frames of the same location after applying the traditional Doppler OCT. The phase value was calculated from the pixels whose intensity was ~15 dB higher than the noise floor. As we can see, due to the tissue movements, the phase difference values vary slowly from $-\pi$ to π along the fast scan direction. The direct application of the UHS-OMAG algorithm leads to unresolvable flow image, presented in Fig. 3(c), from which almost none of the blood flow vessels are distinguishable from the background tissue image. Traditionally, this problem was

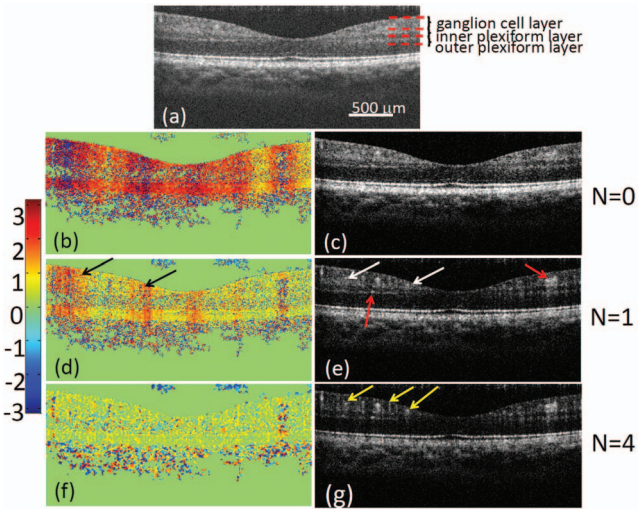

Fig. 3 UHS-OMAG cross-sectional images of the retina around the macular region. (a) Typical cross-sectional structure image, from which three layers (GCL, IPL, and OPL) can be clearly identified. (b) Phase difference map between adjacent B-scans ($N = 0$). (c) UHS-OMAG flow image without phase compensation ($N = 0$). (d) Phase difference map after one time phase compensation ($N = 1$). (e) UHS-OMAG flow image after one time phase compensation ($N = 1$). (f) Phase difference map after high order phase compensation ($N = 4$). (g) UHS-OMAG flow image after high order phase compensation ($N = 4$). The color bar of the phase difference map is from $-\pi$ to π.

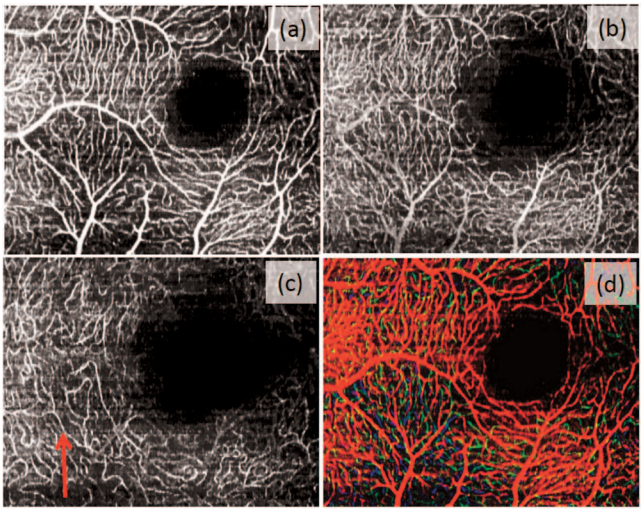

Fig. 4 UHS-OMAG reveals detailed retinal microvasculature network around macular region. (a), (b), and (c) present the blood vessel networks located at the GCL, IPL, and OPL layers, respectively. (d) False-color depth-encoded blood vessel images by integrating (a), (b), and (c) into one image. The red, green, and blue colors correspond to the vessels within the GCL, IP, and OPL layers, respectively.

solved through compensating the phase values resulting from the bulk tissue motion before applying the UHS-OMAG algorithm. Figure 3(d) is the phase difference map after compensating the bulk motion value. Compared to Fig. 3(b), Fig. 3(d) demonstrates much lower phase values due to the tissue motion, indicating that a substantial amount of tissue movements has been compensated during this process. After applying the UHS-OMAG algorithm on the compensated interferograms, the imaging contrast due to the blood flow was improved, as shown in Fig. 3(e). Several blood vessels buried within the retinal tissue bed began to show up, e.g., those pointed by the solid arrows. However for this case, because the tissue movement at some locations was faster than that is resolvable by the Doppler OCT method, the traditional phase-compensation method failed in a number of areas in the image, e.g., those pointed by the black arrows in Fig. 3(d). This is caused by the residual tissue motion that was not compensated by the algorithm, leading to notable motion artifacts in UHS-OMAG flow image [pointed by the white arrows in Fig. 3(e)] that in turn reduces the flow image contrast. These unresolvable phase values could be further compensated through the high order phase compensation method as described in Sec. 3. Figure 3(f) depicts the phase difference map after applying four times the phase compensation method. We can see that almost all the bulk tissue motions, including the phases due to the unresolvable movements demonstrated in Fig. 3(d), were successfully compensated. After applying the UHS-OMAG algorithm at this stage, the flow image contrast was significantly improved, as shown in Fig. 3(g). Compared to the noncompensated flow image [Fig 3(c)] and the flow image using the traditional phase-compensation method [Fig. 3(e)], the blood flow image resulting from the high order phase compensation approach [Fig. 3(g)] reveals much clearer microblood vessels [e.g., those pointed by the arrows in Fig. 2(g)], almost free of the bulk tissue motion artifacts, indicating that the proposed high order phase compensation algorithm is efficient in significantly improving the UHS-OMAG flow image quality when the involuntary movement is inevitable.

However, the image quality improvement using the current motion compensation algorithm is not without price. Repeatedly applying the traditional phase-compensation method on the OCT interferograms requires the increased computational power, which can be a drawback for practical *in vivo* imaging applications. Please note that this increase of computational power does not affect the imaging time for UHS-OMAG to capture the 3D dataset, which should be decoupled from the considerations when imaging the patients.

5.2 *Depth Localized Microvasculature Perfusion Maps Within Retina*

Figure 4 presents the typical vasculature networks segmented from different depth layers within the human retina around the macular region. They were reconstructed from the UHS-OMAG interferogram data captured using the low-resolution imaging probe at the location marked by the yellow square in Fig. 2. The image size is $\sim 4 \times 3$ mm^2 ($X \times Y$), which consisted of 500 pixels in the X direction and 250 pixels in the Y direction. Figures 4(a)–4(c) are the microvasculature networks located at GCL, IPL, and OPL, respectively. These three microvasculature maps demonstrate different vasculature patterns. The large vessels mainly located within the superficial layer [as shown in Fig. 4(a)], and were interconnected through capillary plexus. The weak appearances of the large vessels (artifacts) in Fig. 4(b) are caused by the tailing effect of the light scattering below them (see, for example, a large vessel in the left side in Fig. 3, pointed by the red arrow). The reason for this tailing artifact may be complicated. Briefly, there are two possible causes:

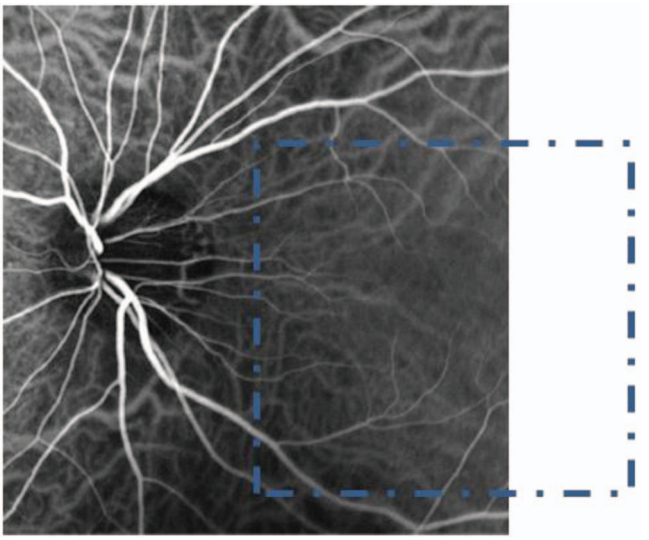

Fig. 5 Fluorescence angiography ocular vasculature map of the healthy volunteer. The blue square indicates the location of retina blood perfusion map obtained by UHS-OMAG system.

1. the multiple scattering of the light within the large blood vessel makes the detected light to have a longer optical path length than it should be. 2. The light backscattered from the positions below the large blood vessel experiences the Doppler effect when it passes through the vessel where the moving blood cells exist. Because the Doppler effect is memorized by the detected light, the UHS-OMAG system sees it as if they were the blood flow signals from beneath the large blood vessel. The exact cause of the tailing artifact deserves a systematic investigation, which is beyond the scope of the current study.

Except those large blood vessels, Fig. 4(b) shows much denser and complicated capillary network than that in Fig. 4(a). Compared to Figs. 4(a) and 4(b), Fig. 4(c) demonstrates relatively sparse and more simple capillary networks. Even a single capillary (e.g., the vessel pointed by the red arrow) could be traced. By combining the vessel networks within these three layers, Fig. 4(d) shows a false color depth-encoded projection view of the microvasculature map within the retina around the macular region. The red, green, and blue colors correspond to the vessel networks located at the GCL, IPL, and OPL layers, respectively. Figure 4 may be helpful in providing, with an intuitive way, the relative locations of different vessel networks. Other than the blood vessel network pattern, a region with no vasculature is identified, which corresponds to the avascular fovea zone, the enlargement of which is a good indicator of diabetic retinopathy.[33]

5.3 *Visualization of Retinal Microvasculature Within a Large Field of View*

In some clinical applications, the ability to visualize the retinal microvasculature network within a large field of view is sometimes critical for an imaging system. Figure 5 is a fluorescence angiography vasculature map captured from the same volunteer. This map could provide the overall information about the status of the volunteer's retinal microvasculature. For the current UHS-OMAG system, the field of view of one 3D scan is 4×3 mm^2 (X direction by Y direction), which is much smaller compared to the region in Fig. 5. To obtain microvasculature maps within a larger field of view comparable to the typical FA

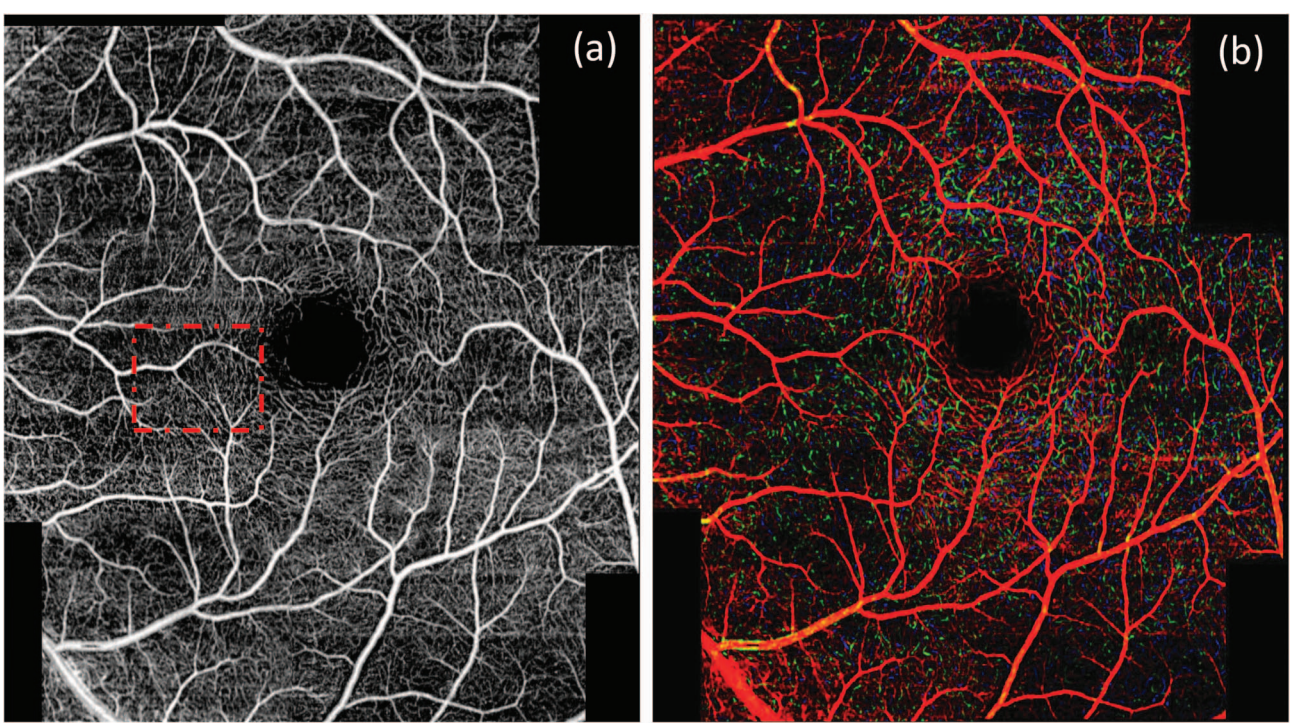

Fig. 6 UHS-OMAG is capable of providing (a) retinal microvasculature maps within a large field of view, and (b) the corresponding color depth-encoded retinal vasculature map (the red, green, and blue colors represent the GCL, IPL, and OPL, respectively).

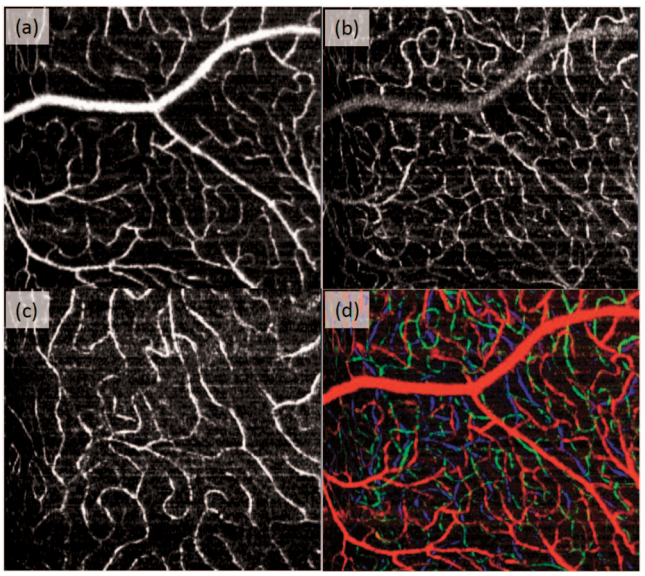

Fig. 7 High resolution UHS-OMAG retinal vasculature network images reveal clear details of the vessel interconnections, particularly for the capillary blood vessels. (a), (b), and (c) present the blood vessel networks located at the GCL, IPL, and OPL layers, respectively. (d) False color depth-encoded blood vessel images by combining the vessels presented in (a), (b), and (c). The red, green, and blue colors correspond to GCL, IPL, and OPL, respectively.

image, we sequentially scanned six locations (corresponding to the areas marked by the squares in Fig. 2). After post-data processing and image stitching, a retinal vasculature map covering a 7×8 mm^2 area was created. The result is demonstrated in Fig. 6. Figure 6(a) is the projection view of the retinal microvasculature network in such a large area (the corresponding location of Fig. 6 is marked by the blue square in Fig. 5). Because these two images, i.e., Figs. 5 and 6, were captured separately, there is a mismatch area on the right side of Fig. 5. Compared to the FA image, the UHS-OMAG reveals not only the big blood vessels but also the abundant capillary blood vessels, which is true for a highly energy-demanding tissue, like the retina. In addition, another advantage of UHS-OMAG is that it can provide depth information of the microvasculature map, which FA is not able to. Based on the depth resolved capability, the blood vessels demonstrated in Fig. 6(a) are color-encoded according to their depth locations. The result is shown in Fig. 6(b). The red, green, and blue colors stand for the GCL, the IPL, and OPL, respectively.

5.4 *High Resolution Retinal Microvasculature Images*

Due to a relatively lower lateral resolution ($\sim$16 μm), Fig. 6 is difficult to reveal the detailed morphological information of the smallest capillaries (between 6 and 8 μm in diameter). To overcome this limitation, we used a higher lateral resolution optical imaging probe in the sample arm to achieve 5 μm lateral resolution for the system. Following the scanning protocol described in Sec. 4 (500 lines in the X-direction covering 1.5 mm; 250 B-frame positions in the Y-direction covering 1.2 mm; 400 frame/s frame rate), a high resolution image of the retinal microvasculature was captured. The corresponding location was marked by the red square in Fig. 2 and also in Fig. 6(a). The results are demonstrated in Fig. 7, where the images clearly speak for themselves. Figures 7(a)–7(c) are the retinal microvasculature networks extracted from the 3D UHS-OMAG flow data set, which represent the vessel networks located at the GCL, IPL, and OPL layers, respectively. Figure 7(d) is the combination of the three layers, with vessels at different layers encoded with different colors (red, green, and blue for GC, IPL, and OPL, respectively). Compared to Figs. 5–7 reveals much clearer morphological information of retinal vasculature networks in different layers. However, the imaging area is smaller than Figs. 5 and 6. In real diagnostic applications on patients, the combination of the high resolution image and the wide field of view image would be very useful. The wide field of view image may be used to find the region of interest where the abnormal blood vessels are located, and the high resolution image can then be used to provide the detailed status of the abnormal blood vessels.

6 Conclusion

We have demonstrated the capability of the new generation UHS-OMAG imaging system to achieve depth-resolved two-dimensional projection views of retinal microvasculature networks. Compared to prior OMAG work, we have made two important improvements to enhance the performance of the current system. The first is that a high speed line scan CMOS camera was employed in the system, providing a 240 kHz A-line scan rate. This camera has enabled us to acquire more A-lines within one B-scan frame at a high frame rate (400 Hz), making it possible to image a larger area on the human retina. The second is that a high order phase compensation algorithm was proposed and implemented to markedly improve the tolerability of the imaging system to the inevitable human eye and head movements during the *in vivo* imaging. With the current UHS-OMAG system, we proposed two different imaging protocols to achieve visualization of human retinal microvasculature networks with targeted goals. The first used a low resolution optical imaging probe in the sample arm to achieve a 4×3 mm^2 scanning area on the human retina. Through combining six scans at the different locations, we have shown that the UHS-OMAG system is capable of visualizing the microvasculature networks within a large field of view (7×8 mm^2), comparable to that of the clinical FA imaging modality. The second used a high resolution ($\sim$5 μm) optical imaging probe in the sample arm for visualization, with a remarkable fidelity, of the detailed microretinal blood vessels in a relatively small area (1.5×1.2 mm^2). We expect that by combining these two imaging protocols, a useful imaging strategy may be formed in the clinical utility of the UHS-OMAG technique, because the former may be used to obtain the overall status of the global retinal microvasculature while the latter can be used to obtain the detailed microvasculature information. The promising imaging results delivered by the UHS-OMAG system demonstrate great potential in the diagnosis of vasculature related eye diseases, such as diabetic retinopathy and AMD.

Acknowledgments

This work was supported in part by research grants from the National Heart, Lung, and Blood Institute (R01 HL093140),

National Institute of Biomedical Imaging and Bioengineering (R01 EB009682), the American Heart Association (0855733G), and Research to Prevent Blindness.

The content is solely the responsibility of the authors and does not necessarily represent the official views of grant giving bodies.

References

1. P. K. Yu, C. Balaratnasingam, S. J. Cringle, I. L. McAllister, J. Provis, and D.-Y. Yu, "Microstructure and network organization of the microvasculature in the human macula," *Invest. Ophthalmol. Visual Sci.* **51**, 6735–6743 (2010).
2. J. Flammer, S. Orgul, V. P. Costa, N. Orzalesi, G. K. Krieglstein, L. M. Serra, J.-P. Renard, and E. Stefansson, "The impact of ocular blood flow in glaucoma," *Prog. Retin. Eye Res.* **21**, 359–393 (2002).
3. V. Patel, S. Rassam, R. Newsom, J. Wiek, and E. Kohner, "Retinal blood flow in diabetic retinopathy," *BMJ* **305**(6855), 678–683 (1992).
4. E. Friedman, "A hemodynamic model of the pathogenesis of age-related macular degeneration," *Am. J. Ophthalmol.* **124**, 677–682 (1997).
5. D. Huang, E. A. Swanson, C. P. Lin, J. S. Schuman, W. G. Stinson, W. Chang, M. R. Hee, T. Flotte, K. Gregory, C. A. Puliafito, and J. G. Fujimoto, "Optical coherence tomography," *Science* **254**(5035), 1178–1181 (1991).
6. A. F. Fercher, W. Drexler, C. K. Hitzenberger, and T. Lasser, "Optical coherence tomography – principles and applications," *Rep. Prog. Phys.* **66**(2), 239–303 (2003).
7. P. H. Tomlins and R. K. Wang, "Theory, development and applications of optical coherence tomography," *J. Phys. D: Appl. Phys.* **38**(15), 2519–2535 (2005).
8. Y. H. Zhao, Z. P. Chen, C. Saxer, S. H. Xiang, J. F. de Boer, and J. S. Nelson, "Phase-resolved optical coherence tomography and optical Doppler tomography for imaging blood flow in human skin with fast scanning speed and high velocity sensitivity," *Opt. Lett.* **25**(2), 114–116 (2000).
9. S. Jiao, R. Knighton, X. Huang, G. Gregori, and C. A. Puliafito, "Simultaneous acquisition of sectional and fundus ophthalmic images with spectral-domain optical coherence tomography," *Opt. Express* **13**, 444–452 (2005).
10. B. R. White, M. C. Pierce, N. Nassif, B. Cense, B. H. Park, G. J. Tearney, B. E. Bouma, T. C. Chen, and J. F. de Boer, "In vivo dynamic human retinal blood flow imaging using ultra-high-speed spectral domain optical coherence tomography," *Opt. Express* **11**(25), 3490–3497 (2003).
11. R. Leitgeb, L. Schmetterer, W. Drexler, A. Fercher, R. Zawadzki, and T. Bajraszewski, "Real-time assessment of retinal blood flow with ultrafast acquisition by color Doppler Fourier domain optical coherence tomography," *Opt. Express* **11**(23), 3116–3121 (2003).
12. S. Makita, Y. Hong, M. Yamanari, T. Yatagai, and Y. Yasuno, "Optical coherence angiography," *Opt. Express* **14**(17), 7821–7840 (2006).
13. Y. K. Tao, K. M. Kennedy, and J. A. Izatt, "Velocity-resolved 3D retinal microvessel imaging using single-pass flow imaging spectral domain optical coherence tomography," *Opt. Express* **17**(5), 4177–4188 (2009).
14. A. H. Bachmann, M. L. Villiger, C. Blatter, T. Lasser, and R. A. Leitgeb, "Resonant Doppler flow imaging and optical vivisection of retinal blood vessels," *Opt. Express* **15**(2), 408–422 (2007).
15. M. Szkulmowski, A. Szkulmowska, T. Bajraszewski, A. Kowalczyk, and M. Wojtkowski, "Flow velocity estimation using joint spectral and time domain optical coherence tomography," *Opt. Express* **16**(9), 6008–6025 (2008).
16. A. Mariampillai, B. A. Standish, E. H. Moriyama, M. Khurana, N. R. Munce, M. K. K. Leung, J. Jiang, A. Cable, B. C. Wilson, I. A. Vitkin, and V. X. D. Yang, "Speckle variance detection of microvasculature using swept-source optical coherence tomography," *Opt. Lett.* **33**(13), 1530–1532 (2008).
17. B. J. Vakoc, R. M. Lanning, J. A. Tyrrell, T. P. Padera, L. A. Bartlett, T. Stylianopoulos, L. L. Munn, G. J. Tearney, D. Fukumura, R. K. Jain, and B. E. Bouma, "Three-dimensional microscopy of the tumor microenvironment in vivo using optical frequency domain imaging," *Nat. Med.* **15**(10), 1219–1223 (2009).
18. L. Yu and Z. Chen, "Doppler variance imaging for three-dimensional retina and choroid angiography," *J. Biomed. Opt.* **15**(1), 016029 (2010).
19. J. Fingler, R. J. Zawadzki, J. S. Werner, D. Schwartz, and S. E. Fraser, "Volumetric microvascular imaging of human retina using optical coherence tomography with a novel motion contrast technique," *Opt. Express* **17**(24), 22190–22200 (2009).
20. D. Y. Kim, J. Fingler, J. S. Werner, D. M. Schwartz, S. E. Fraser, and R. J. Zawadzki, "In vivo volumetric imaging of human retinal circulation with phase-variance optical coherence tomography," *Biomed. Opt. Express* **2**(6) 1504–1513 (2011).
21. J. Enfield, E. Jonathan, and M. Leahy, "In vivo imaging of the microcirculation of the volar forearm using correlation mapping optical coherence tomography (cmOCT)," *Biomedical Opt. Express* **2**(5), 1184–1193 (2011).
22. T. Schmoll, A. S. G. Singh, C. Blatter, S. Schriefl, C. Ahlers, U. Schmidt-Erfurth, and R. A. Leitgeb, "Imaging of the parafoveal capillary network and its integrity analysis using fractal dimension," *Biomedical Opt. Express* **2**(5) 1159–1168 (2011).
23. R. K. Wang and Z. Ma, "Real time flow imaging by removing texture pattern artifacts in ultrafast spectral domain optical Doppler tomography," *Opt. Lett.* **31**, 3001–3003 (2006).
24. S. Makita, F. Jaillon, M. Yamanari, M. Miura, and Y. Yasuno, "Comprehensive in vivo micro-vascular imaging of human eye by dual-beam-scan Doppler optical coherence angiography," *Opt. Express* **19**, 1271–1283 (2011).
25. S. Zotter, M. Pircher, T. Torzicky, M. Bonesi, E. Götzinger, R. A. Leitgeb, and C. K. Hitzenberger, "Visualization of microvasculature by dual-beam phase-resolved Doppler optical coherence tomography," *Opt. Express* **19**(2), 1217–1227 (2011).
26. R. K. Wang, S. L. Jacques, Z. H. Ma, S. Hanson, and A. Gruber, "Three dimensional optical angiography," *Opt. Express* **15**, 4083–4097 (2007).
27. L. An and R. K. Wang, "In vivo volumetric imaging of vascular perfusion within human retina and choroids with optical micro-angiography," *Opt. Express* **16**(15), 11438–11452 (2008).
28. L. An, H. M. Subhush, D. J. Wilson, and R. K. Wang, "High-resolution wide-field imaging of retinal and choroidal blood perfusion with optical microangiography," *J. Biomed. Opt.* **15**(2), 026011 (2010).
29. R. K. Wang, L. An, S. Saunders, and D. J. Wilson, "Optical microangiography provides depth-resolved images of directional ocular blood perfusion in posterior eye segment," *J. Biomed. Opt.* **15**(2), 020502 (2010).
30. L. An, J. Qin, and R. K. Wang, "Ultrahigh sensitive optical microangiography for in vivo imaging of microcirculations within human skin tissue beds," *Opt. Express* **18**(8), 8220–8228 (2010).
31. R. K. Wang, L. An, P. Francis, and D. J. Wilson, "Depth-resolved imaging of capillary networks in retina and choroid using ultrahigh sensitive optical microangiography," *Opt. Lett.* **35**(9), 1467–1469 (2010).
32. R. K. Wang and L. An, "Doppler optical micro-angiography for volumetric imaging of vascular perfusion invivo," *Opt. Express* **17**(11), 8926–8940 (2009).
33. G. H. Bresnick, R. Condit, S. Syrjala, M. Palta, A. Groo, and K. Korth, "Abnormalities of the foveal avascular zone in diabetic retinopathy," *Arch. Ophthalmol.* **102**(9), 1286–1293 (1984).